Discrete dislocation plasticity analysis of the wedge indentation of films

Balint, D. S.; Deshpande, V. S.; Needleman, A.; Van der Giessen, E.

Published in:
Journal of the Mechanics and Physics of Solids

DOI:
10.1016/j.jmps.2006.07.004

Publication date:
2006

Available online at www.sciencedirect.com
ScienceDirect
Journal of the Mechanics and Physics of Solids
54 (2006) 2281–2303

JOURNAL OF THE MECHANICS AND PHYSICS OF SOLIDS

www.elsevier.com/locate/jmps

Discrete dislocation plasticity analysis of the wedge indentation of films

D.S. Balint[a], V.S. Deshpande[a,*], A. Needleman[b], E. Van der Giessen[c]

[a]*Department of Engineering, Cambridge University, Trumpington Street, Cambridge CB2 1PZ, UK*
[b]*Division of Engineering, Brown University, Providence, RI 02912, USA*
[c]*Department of Applied Physics, University of Groningen, Nyenborgh 4, 9747 AG Groningen, The Netherlands*

Received 2 March 2006; received in revised form 23 June 2006; accepted 3 July 2006

Abstract

The plane strain indentation of single crystal films on a rigid substrate by a rigid wedge indenter is analyzed using discrete dislocation plasticity. The crystals have three slip systems at $\pm 35.3^\circ$ and 90° with respect to the indentation direction. The analyses are carried out for three values of the film thickness, 2, 10 and 50 μm, and with the dislocations all of edge character modeled as line singularities in a linear elastic material. The lattice resistance to dislocation motion, dislocation nucleation, dislocation interaction with obstacles and dislocation annihilation are incorporated through a set of constitutive rules. Over the range of indentation depths considered, the indentation pressure for the 10 and 50 μm thick films decreases with increasing contact size and attains a contact size-independent value for contact lengths $A > 4\,\mu m$. On the other hand, for the 2 μm films, the indentation pressure first decreases with increasing contact size and subsequently increases as the plastic zone reaches the rigid substrate. For the 10 and 50 μm thick films sink-in occurs around the indenter, while pile-up occurs in the 2 μm film when the plastic zone reaches the substrate. Comparisons are made with predictions obtained from other formulations: (i) the contact size-independent indentation pressure is compared with that given by continuum crystal plasticity; (ii) the scaling of the indentation pressure with indentation depth is compared with the relation proposed by Nix and Gao [1998. Indentation size effects in crystalline materials: a law for strain gradient plasticity. J. Mech. Phys. Solids 43, 411–423]; and (iii) the computed contact area is compared with

*Corresponding author.
E-mail address: vsd@eng.cam.ac.uk (V.S. Deshpande).

doi:10.1016/j.jmps.2006.07.004

that obtained from the estimation procedure of Oliver and Pharr [1992. An improved technique for determining hardness and elastic-modulus using load and displacement sensing indentation experiments, J. Mater. Res. 7, 1564–1583].

Keywords: Discrete dislocations; Mechanical properties; Size effects; Plasticity; Indentation

1. Introduction

Indentation is used extensively to measure the hardness of materials. The objective is usually to draw inferences about the mechanical properties (e.g. modulus, yield strength) of the material. Tabor (1951) and Johnson (1970) established relationships between hardness as measured by conical (or pyramidal) and spherical indenters and the stress–strain behavior in the regime of "large" indents for which conventional plasticity theory is applicable.

When the contact area is sufficiently small, in micro- and nano-indentation, hardness values are much increased, giving rise to the well-known indentation size effect, e.g. Ma and Clarke (1995), Poole et al. (1996), Swadener et al. (2002), which cannot be accounted for by conventional plasticity. A clear understanding of the indentation size effect and its connection with material strength is especially important in modern applications involving thin films and multi-layers since nano- and micro-indentation are frequently the only means of measuring strength, see, for example, Gouldstone et al. (2000) and Lou et al. (2003). Readers are referred to Freund and Suresh (2004) for further details and references. Simulations based on continuum elastic–plastic analyses have typically been used to extract the plastic properties of the thin films from these nano-indentation measurements (Bhattacharya and Nix, 1988). However, these continuum calculations are unable to account for the size effects typically observed in the experiments.

The indentation size effect has been one of the motivations underlying the development of a plasticity theory for the micron scale and there is a large literature concerned with modeling indentation size effects using various non-local plasticity theories, e.g. Begley and Hutchinson (1998), Wei and Hutchinson (2003) and Qu et al. (2006). Nix and Gao (1998) presented a simple analytical formula for the indentation size effect based on the idea of geometrically necessary dislocations. With the characteristic length scale in the model used as a fitting parameter, experimental data have been fit reasonably well, see, for example, Lou et al. (2003). Similarly, other modeling frameworks including molecular dynamics (Horstemeyer et al., 2001), interatomic potential finite element method (Zhu et al., 2003) and coupled atomistics and discrete dislocation plasticity (Miller et al., 2004) have also been used to investigate the indentation response of crystalline solids. However, the "plastic zones" in indentation problems are sufficiently large that current computational capabilities restrict the molecular dynamics simulations to the nano-indentation regime.

In principle, discrete dislocation plasticity should be able to bridge the gap between the nano-indentation and the size-independent continuum regimes. An early three-dimensional discrete dislocation plasticity simulation of the nano-indentation of copper crystals was reported by Fivel et al. (1998). While there was good qualitative agreement between the experimentally observed and predicted dislocation structures, the indentation depths in the simulations were too small (50 nm) for the indentation size effect to be explicitly

investigated. Two-dimensional discrete dislocation plasticity simulations of indentation (Kreuzer and Pippan, 2004, 2005; Polonsky and Keer, 1996) have shown size effects for both sinusoidal- and wedge-shaped indenters. In these simulations, "low source density" materials were considered with the plasticity size effect mainly resulting from source-limited plasticity. Widjaja et al. (2005, 2006) reported on two-dimensional simulations for the cylindrical indentation of materials with a wide range of source densities. Over the range of indentation depths considered in these studies, the increasing hardness with increasing indentation depth associated with sharp indenters was not obtained and the cylinder radius played a dominant role. This is consistent with experimental observations, see, for example, Swadener et al. (2002).

In previous discrete dislocation simulations, the indentation depths reached were not sufficiently large to observe the transition from a size-dependent hardness to a size-independent "continuum" hardness. Here, we consider: (i) the effect of film thickness on indentation hardness; (ii) the scaling of the hardness in the size-dependent regime; and (iii) the transition from a size-dependent to a size-independent hardness. Our study employs the discrete dislocation plasticity formulation of Van der Giessen and Needleman (1995), which has been extensively used to predict plasticity size effects in a variety of situations, including those in bending (Cleveringa et al., 1999) and in the uniaxial compression/tension of single crystals (Deshpande et al., 2005).

2. Discrete dislocation formulation

A plane strain analysis of the wedge indentation of a single crystal film of thickness h and length L rigidly bonded to a rigid substrate is carried out. Plasticity in the film is described by the collective motion of discrete edge dislocations on specified slip planes. Complete sticking contact between the rigid indenter and the film is assumed.

The boundary value problem analyzed is sketched in Fig. 1a. The single crystal film is elastically isotropic with Young's modulus E and Poisson's ratio ν, and has three potentially active slip systems at angles $\phi^{(\alpha)}$ ($\alpha = 1, 2, 3$) with respect to the x_2-axis. Plasticity originates from the motion of edge dislocations, represented as line singularities in an elastic medium, that can nucleate and glide on the active slip planes.

At each stage of loading, the stress and deformation state is computed using superposition (Van der Giessen and Needleman, 1995) of a singular field and an image field. The singular field ($\tilde{}$) associated with the N dislocations is calculated analytically from the isotropic linear elastic dislocation fields in a half-space $x_2 \leqslant h$ (Freund, 1994). The complete solution is obtained by adding a smooth image field ($\hat{}$) that ensures that the

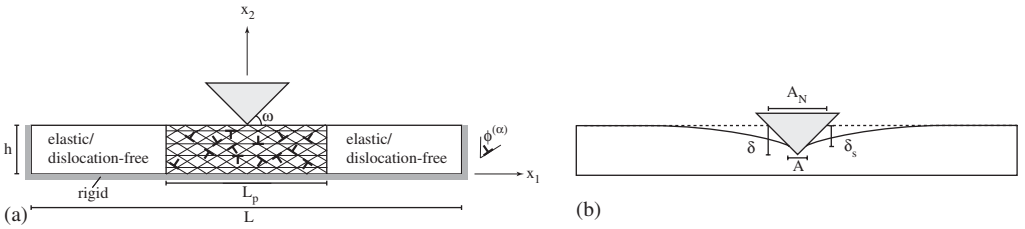

Fig. 1. (a) Sketch of the indentation boundary value problem analyzed. (b) The definitions of the actual contact length A, the nominal contact length A_N, the indentation depth δ and sink-in δ_s.

boundary conditions (see Section 2.1 for details) are satisfied. The displacements u_i, strains ε_{ij}, and stresses σ_{ij} are written as

$$u_i = \hat{u}_i + \tilde{u}_i, \quad \varepsilon_{ij} = \hat{\varepsilon}_{ij} + \tilde{\varepsilon}_{ij}, \quad \sigma_{ij} = \hat{\sigma}_{ij} + \tilde{\sigma}_{ij}, \tag{1a}$$

where the ($\tilde{}$) field is the sum of the fields of the individual dislocations in their current positions, i.e.

$$\tilde{u}_i = \sum_{J=1}^{N} \tilde{u}_i^{(J)}, \quad \tilde{\varepsilon}_{ij} = \sum_{J=1}^{N} \tilde{\varepsilon}_{ij}^{(J)}, \quad \tilde{\sigma}_{ij} = \sum_{J=1}^{N} \tilde{\sigma}_{ij}^{(J)}. \tag{1b}$$

The image field is obtained by solving a linear elastic boundary value problem using finite elements with the boundary conditions changing as the dislocation structure evolves.

At the beginning of a calculation, the crystal is stress- and dislocation-free. The long-range interactions of the dislocations are accounted for through their elastic fields while constitutive rules are prescribed for short-range interactions. Dislocation dipoles with Burgers vectors $\pm b$ are nucleated at point sources, that simulate Frank–Read sources, randomly distributed on discrete slip planes. Nucleation occurs when the magnitude of the resolved shear stress at the source exceeds a critical value τ_{nuc} during a time period t_{nuc}. The sign of the dipole is determined by the sign of the resolved shear stress along the slip plane while the distance between the two dislocations at nucleation, L_{nuc}, is taken such that the attractive stress that the dislocations exert on each other is equilibrated by a shear stress of magnitude τ_{nuc}. After nucleation, the dislocations glide apart, driven by the Peach–Koehler force acting on them, given by

$$f^{(I)} = m_i^{(I)} \left[\hat{\sigma}_{ij} + \sum_{J \neq I} \tilde{\sigma}_{ij}^{(J)} + \Sigma_{ij}^{(I)} \right] b_j^{(I)}, \tag{2}$$

where $m_i^{(I)}$ is the unit normal to the slip system on which the dislocation with Burgers vector $b_j^{(J)}$ resides and $\Sigma_{ij}^{(I)}$ is the image field on dislocation I due to the traction-free surface, i.e. the difference between the half-space and infinite medium fields. The magnitude of the glide velocity $V_{\text{gln}}^{(I)}$ along the slip direction of dislocation I is taken to be linearly related to the Peach–Koehler force $f^{(I)}$ through the drag relation

$$V_{\text{gln}}^{(I)} = \frac{1}{B} f^{(I)}, \tag{3}$$

where B is the drag coefficient. Annihilation of two oppositely signed dislocations on a slip plane occurs when they are within a material-dependent critical annihilation distance L_{e}. Obstacles to dislocation motion are modeled as points associated with a slip plane which pin dislocations that attempt to pass through them. An obstacle releases a pinned dislocation when the Peach–Koehler force on the obstacle exceeds $\tau_{\text{obs}} b$, where τ_{obs} is the obstacle strength.

2.1. Boundary conditions

Effects of geometry changes on the momentum balance and lattice rotations are neglected. However, the contact between the rigid wedge (whose faces are inclined at an angle ω with respect to the x_1-axis) and the film is based on the deformed film surface. At the current stage of deformation, the depth of the indentation is denoted by δ and the

contact length A is defined as the range between the smallest and the largest values of x_1 where the indenter touches the deformed surface. In general, A differs from the nominal contact length $A_N \equiv 2\delta/\tan\omega$ due to sink-in or pile-up as sketched in Fig. 1b, but it does not account for surface roughness which, as shown by Widjaja et al. (2006), can lead to a significantly smaller contact area in some circumstances and especially for sharp indenters. Perfect sticking is assumed as soon as the wedge comes in contact with the film so the rate boundary conditions applied are

$$\dot{u}_1 = 0, \quad \dot{u}_2 = -\dot{\delta} \quad \text{on } S_{\text{contact}}, \tag{4a}$$

where S_{contact} denotes the portion of the deformed surface $x_2 = h$ in contact with the wedge and the over-dot signifies time differentiation. The other boundary conditions are

$$\dot{u}_1 = \dot{u}_2 = 0, \quad \text{on } x_1 = \pm L/2 \text{ and on } x_2 = 0, \tag{4b}$$

and $\dot{T}_1 = \dot{T}_2 = 0$ on $x_2 = h \notin S_{\text{contact}}$. Here, $T_i = \sigma_{ij} n_j$ is the surface traction on a surface with outward normal n_j. The applied load is computed as

$$F = -\int_{-L/2}^{L/2} T_2(x_1, h)\, \mathrm{d}x_1, \tag{5}$$

to give the indentation force versus depth δ response. A time step of $\Delta t = 0.5$ ns is needed to resolve the dislocation dynamics. Unless otherwise specified, in order to limit the computation time, a rather high loading rate $\dot{\delta} = 0.4\,\text{ms}^{-1}$ is employed in most of the calculations reported below. Some additional calculations at a reduced indentation rate of $\dot{\delta} = 0.04\,\text{ms}^{-1}$ are also reported.

2.2. Geometry and material properties

Calculations were performed for films of thickness $h = 2$, 10 and 50 μm indented by $\omega = 5^\circ$ and 10° wedges. These wedge angles are smaller than those representative of indenters employed in most experimental studies (e.g. Berkovich or Vickers): larger values of ω result in large contact area jumps in the discrete dislocation calculations and we restrict this study to $\omega \leqslant 10^\circ$. Dislocation activity in a film of length $L = 1000$ μm was restricted to a process region of length $L_p = 50$ μm. The calculations were terminated before dislocations reached the boundaries $x_1 = \pm L_p/2$ and thus the effect of the process region is to restrict the indentation depths attained in the calculations rather than affect the results presented. The finite element mesh was highly refined in a 30 μm × h region around the indenter tip and usually consisted of 180 × 100 bilinear elements with a typical mesh size of about 0.01 μm in a central 1 μm × 1 μm region. This ensured that the contact was accurately modeled and that the gradients in the ($\hat{}$) fields due to the indentation were accurately captured.

Unless otherwise specified, the crystals have the following properties. The film material has Young's modulus $E = 70$ GPa and Poisson's ratio $\nu = 0.33$ and at the beginning of a calculation is stress- and dislocation-free with slip systems at $\phi^{(\alpha)} = \pm 35.3^\circ$ and 90° with respect to the x_2-axis (this corresponds to the slip system orientation in the BCC crack problem in Rice, 1987). Dislocation sources are randomly distributed on slip planes spaced $100b$ apart, with a density $\rho_{\text{nuc}} = 48\,\mu\text{m}^{-2}$. Each source is randomly assigned a nucleation strength τ_{nuc} from a Gaussian distribution with average $\bar{\tau}_{\text{nuc}} = 50$ MPa and standard deviation 10 MPa; the nucleation time $t_{\text{nuc}} = 10$ ns for all sources. The magnitude of the

Burgers vector is taken to be $b = 0.25\,\text{nm}$ for all dislocations. The distance between the two dislocations at nucleation, L_{nuc}, scales with the source strength and, on an average, is $L_{\text{nuc}} = 0.03\,\mu\text{m}$. The drag coefficient for dislocation motion is $B = 10^{-4}\,\text{Pa s}$ and the annihilation distance is $L_e = 6b$. Obstacles of strength $\tau_{\text{obs}} = 150\,\text{MPa}$ are randomly distributed with a density $\rho_{\text{obs}} = 98\,\mu\text{m}^{-2}$. In addition to this reference crystal, a few simulations on a crystal with a low density of sources and obstacles are also reported. These low source density (LSD) crystals have $\rho_{\text{nuc}} = 9\,\mu\text{m}^{-2}$ and $\rho_{\text{obs}} = 18\,\mu\text{m}^{-2}$ and all other properties the same as in the reference crystal case.

2.3. Tensile response

The tensile stress–strain responses of the reference and LSD single crystal materials are shown in Fig. 2a and b, respectively. These calculations were carried out on tensile bars having widths $w = 1.0$–$8.0\,\mu\text{m}$ and length $L = 3w$. As shown in the inset of Fig. 2a, the three slip systems of the single crystal are inclined at $\phi^{(\alpha)} = \pm 35.3^\circ$ and 90° with respect to the tensile axis, so that the tensile response is probed in the direction of indentation. The computations were performed with an imposed nominal strain rate of $\dot{\bar{\varepsilon}} = 2000\,\text{s}^{-1}$; see Cleveringa et al. (1999) for details of such calculations. The stress–strain behavior is linear up to a yield strength and then after a transient, the overall behavior is essentially non-hardening. For the range of specimen sizes considered here, the tensile flow strength of the reference crystals is approximately independent of the specimen size, while the LSD crystal shows a noticeable size effect. However, from the results in Deshpande et al. (2005), it is expected that the tensile strength of the reference crystals will eventually increase with decreasing specimen size. The tensile flow strength $\bar{\sigma}$, identified as the average stress between $0.004 \leqslant \bar{\varepsilon} \leqslant 0.005$ of the $w = 8\,\mu\text{m}$ crystal, is approximately 60 and 50 MPa for the reference and LSD crystals, respectively.

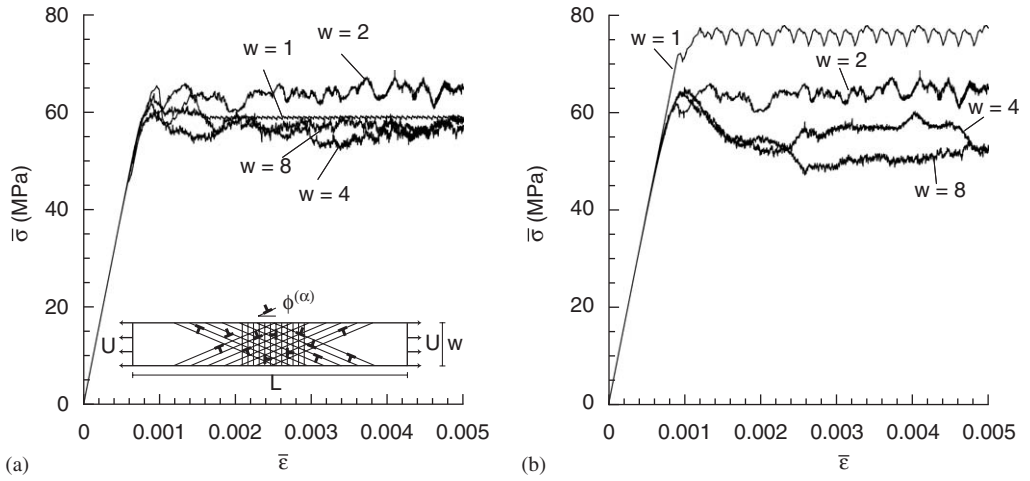

Fig. 2. The tensile stress versus strain response of the (a) reference ($\rho_{\text{src}} = 48\,\mu\text{m}^{-2}$, $\rho_{\text{obs}} = 98\,\mu\text{m}^{-2}$) and (b) low source density ($\rho_{\text{src}} = 9\,\mu\text{m}^{-2}$, $\rho_{\text{obs}} = 18\,\mu\text{m}^{-2}$) crystals. The responses are shown for four selected specimen sizes w (dimensions in μm) in each case and the tensile boundary value problem is as sketched in the inset in (a).

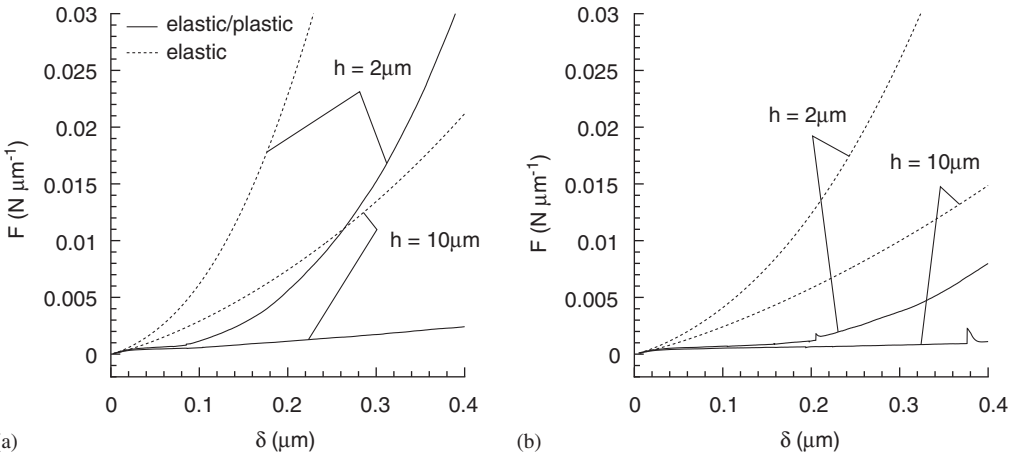

Fig. 3. Indentation force versus applied indentation depth for the (a) $\omega = 5^\circ$ and (b) $\omega = 10^\circ$ wedges. Results are shown for two selected film thicknesses h and both the elastic and discrete dislocation predictions for the reference material are included.

3. Indentation response of the reference crystal films

The indentation force F versus applied indentation depth δ response of the $h = 2$ and 10 μm films is plotted in Fig. 3a and b for the $\omega = 5^\circ$ and 10° indenters, respectively. Predictions for elastic films (i.e. without any dislocation activity) are also included for reference purposes. The indentation force increases approximately quadratically with displacement in all cases. For a given indentation depth, the indentation force increases with decreasing film thickness and increasing wedge angle ω. A comparison with the indentation forces for the purely elastic film reveals that the plasticity caused by the dislocation activity significantly relaxes the stresses in the films, thus reducing the indentation force.

The variation of the actual contact length[1] A with the applied displacement δ is plotted in Fig. 4a and b for the $\omega = 5^\circ$ and 10° wedges, respectively. Results are included in Fig. 4 for all three film thicknesses. For reference purposes, the variation of the nominal contact length, $A_N \equiv 2\delta/\tan\omega$, with displacement is also included in Fig. 4. There are large jumps (much larger than the finite element mesh size) in the contact length. These jumps occur because material sink-in results in a portion of the deformed film surface outside the contact length becoming nearly parallel to the surface of the wedge indenter. Thus, continued indentation results in the contact length increasing in bursts (the spikes in the force versus displacement curves in Fig. 3 correspond to these jumps in the contact length). The prediction of the A versus δ relation for a second realization of sources and obstacles (same initial densities as the reference case) is included in Fig. 4b for the $h = 10$ μm film indented by the $\omega = 10^\circ$ wedge. It is clear from a comparison of the predictions for the two realizations that while the general trends are similar for both realizations, the jumps are stochastic in nature and depend on the details of the initial source and obstacle distributions.

[1]What is termed the actual contact length here is referred to as the end-to-end contact length in Widjaja et al. (2006).

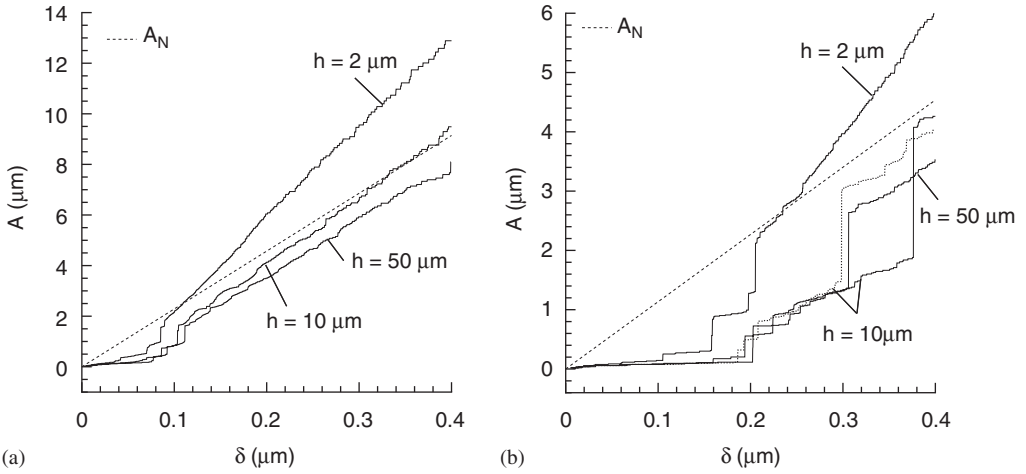

Fig. 4. The relation between the actual contact length A and indentation depth δ for indentation of the reference material with the (a) $\omega = 5^\circ$ and (b) $\omega = 10^\circ$ wedges. Results are shown for three film thicknesses h. The prediction for a second realization of the reference material is included in (b) for the $h = 10\,\mu$m film (dotted curve).

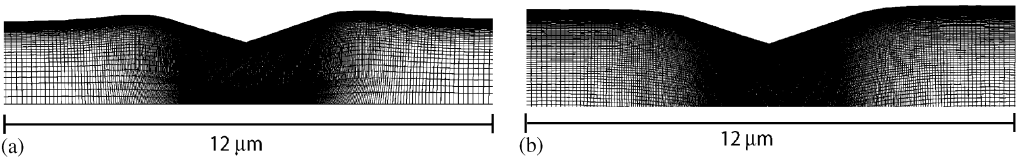

Fig. 5. The deformed mesh (displacements magnified by a factor of 2) in the $\omega = 10^\circ$ wedge indentation of the (a) $h = 2\,\mu$m and (b) $h = 50\,\mu$m films of the reference material. The meshes are shown at the instant when the actual contact length $A = 4\,\mu$m.

The actual contact length A is less than the nominal contact length for the $h = 10$ and $50\,\mu$m films (especially so for the $\omega = 10^\circ$ indenter) while $A > A_N$ for the $h = 2\,\mu$m films at indentation depths greater than 0.1 and $0.2\,\mu$m for the $\omega = 5^\circ$ and 10° indenters, respectively. This is a result of material pile-up for the $h = 2\,\mu$m film and sink-in for the thicker films. To illustrate this, deformed meshes for the $\omega = 10^\circ$ indentation of the $h = 2$ and $50\,\mu$m films are shown in Fig. 5a and b, respectively, at the instant when the actual contact length $A = 4\,\mu$m. These figures show material pile-up for the $2\,\mu$m film and sink-in for the $50\,\mu$m film. However, it is worth noting that material sink-in occurs for small indentation depths even in the $h = 2\,\mu$m films (resulting in $A < A_N$, see Fig. 4) and pile-up begins when the plastic zone under the indenter reaches the rigid substrate at $x_2 = 0$. Pile-up may eventually occur in the 10 and $50\,\mu$m films, albeit at much larger indentation depths than considered here. In order to explore the effect of the side constraint in Eq. (4b) on the evolution of pile-up, calculations were carried out with traction-free boundary conditions on $x_1 = \pm L/2$. This change in boundary conditions had no effect on the development of pile-up, indicating that material pile-up does result from the plastic zone extending to the bottom surface of the film, $x_2 = 0$, and is not a consequence of the side constraint.

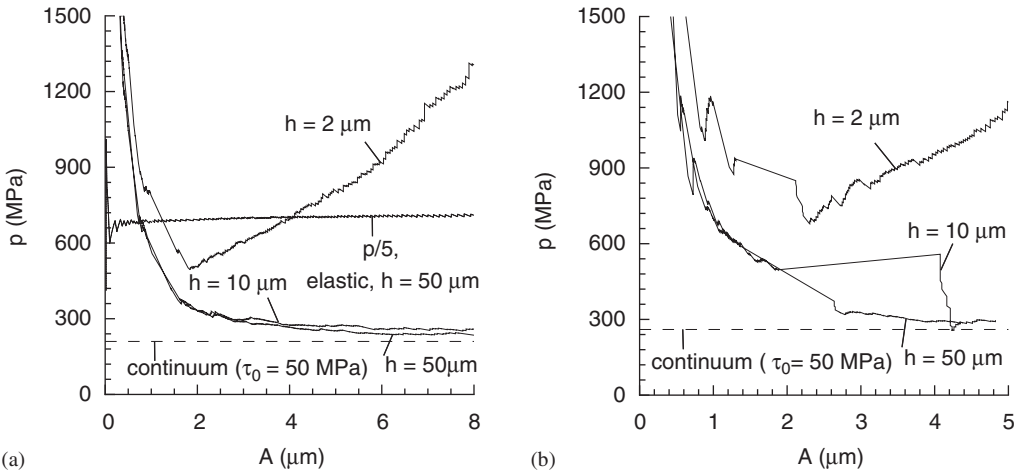

Fig. 6. The indentation pressure p versus actual contact length A relation for indentation of the reference material with the (a) $\omega = 5^\circ$ and (b) $\omega = 10^\circ$ wedges. Results are shown for three film thicknesses h. The continuum predictions of the nominal indentation pressure for a large crystal are also included. In addition, the indentation pressure for an elastic material is also shown in (a) with p divided by five to fit the scale.

The indentation pressure p is defined as the ratio of the indentation force and the actual contact length, viz.

$$p = \frac{F}{A}. \tag{6}$$

The indentation pressure versus actual contact length relation is plotted in Fig. 6a and b for the $\omega = 5^\circ$ and 10° indenters, respectively. The indentation pressure versus contact length relation for the elastic $h = 50\,\mu\text{m}$ film indented by the $\omega = 5^\circ$ wedge is also included in Fig. 6a. No length scale exists in the elastic problem (over the indentation depths considered here) and thus we expect no size effect in the elastic problem. The numerical simulations correctly predict this size independence for $A > 0.05\,\mu\text{m}$: for smaller contact lengths, the numerical length scale introduced by the finite element discretization affects the results. Convergence studies carried out to determine the effect of the numerical length scale introduced by the finite element discretization on the elastic–plastic results revealed that further mesh refinement only affected the results for contact depths of four to five times the element length (i.e. $\delta \approx 0.05\,\mu\text{m}$). These data are excluded from Fig. 6 and the elastic–plastic results presented in Fig. 6 are over the range where the simulations are essentially mesh size-independent.

The results in Fig. 6 show that the indentation pressure decreases with increasing contact length, before leveling off in the $h = 10$ and $50\,\mu\text{m}$ films at $p \approx 300\,\text{MPa}$ for contact lengths $A > 4\,\mu\text{m}$. The indentation pressure versus contact length relations for the $h = 10$ and $50\,\mu\text{m}$ films are almost identical.[2] Bouvier and Needleman (2006) recently reported continuum crystal plasticity calculations for wedge indentation of single crystals and we repeated their calculations for the crystallographic orientation and wedge geometries used

[2]The differences between the $h = 10$ and $50\,\mu\text{m}$ responses in Fig. 6b are a result of jumps in the actual contact length which to a large extent are stochastic in nature. However, the indentation force versus indentation depth curves for these two cases are almost identical.

here with a slip system flow strength $\tau_0 = 50$ MPa and no material hardening. The nominal indentation pressures predicted by the continuum crystal plasticity calculations are included in Fig. 6. The discrete dislocation predictions asymptote towards the continuum crystal plasticity indentation pressure limits that are size-independent.

The differences between the continuum and discrete dislocation predictions are further highlighted by comparing the distributions of the quantity

$$\Gamma = \sum_{\alpha=1}^{3} |\gamma^{(\alpha)}|, \tag{7a}$$

where $\gamma^{(\alpha)}$ is given by

$$\gamma^{(\alpha)} = s_i^{(\alpha)} \varepsilon_{ij} m_j^{(\alpha)}. \tag{7b}$$

Here, $s_i^{(\alpha)}$ and $m_j^{(\alpha)}$ are unit vectors tangential and normal, respectively, to slip system α. Since dislocation glide gives rise to a displacement jump across the slip plane, the displacement field is not continuous. In order to visualize the deformation, we evaluate Γ in the discrete dislocation simulations by evaluating the displacements u_i on a uniform grid with cell size 0.25 μm. The strain field ε_{ij} is then obtained by numerical differentiation using bilinear displacement shape functions. Although it is convenient to use Γ for picturing the deformation mode, Γ in Fig. 7a is not a direct measure of slip since $\gamma^{(\alpha)}$ is not the actual slip on slip plane α as it includes contributions from dislocations gliding on all slip systems. On the other hand, for continuum crystal plasticity, Fig. 7b, $\gamma^{(\alpha)} = s_i^{(\alpha)} \varepsilon_{ij}^p m_j^{(\alpha)}$, where ε_{ij}^p is the plastic strain.

Distributions of Γ at an indentation depth $\delta = 0.4$ μm in the $h = 50$ μm film ($\omega = 5^\circ$) are plotted in Fig. 7a and b using the discrete dislocation and continuum crystal plasticity constitutive descriptions, respectively. The values of Γ in Fig. 7a give a measure of slip averaged over approximately 10 slip planes (the grid size used to evaluate strain is 0.25 μm while the slip plane spacing in the discrete dislocation simulations is 0.025 μm). The discrete dislocation plasticity results give a larger "plastic" zone than the continuum

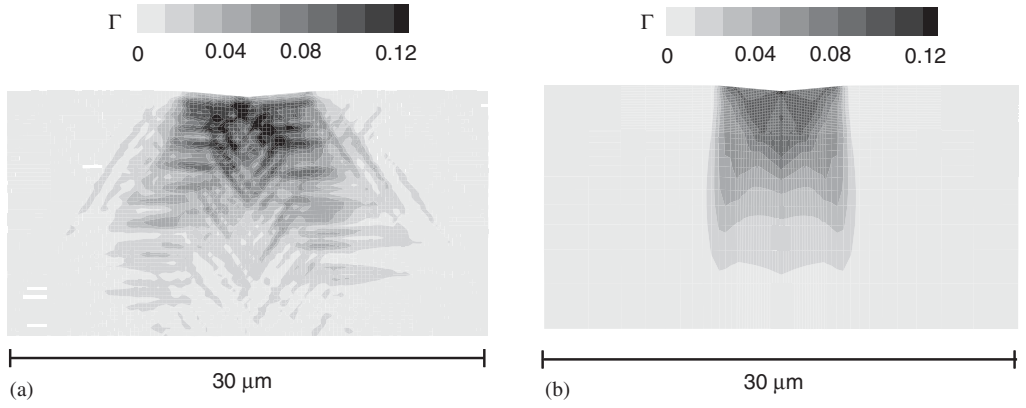

Fig. 7. Distribution of the total slip Γ in the $h = 50$ μm film indented by the $\omega = 5^\circ$ wedge indenter to an indentation depth $\delta = 0.4$ μm ($A = 7.5$ μm). (a) Discrete dislocation prediction for the reference material and (b) continuum crystal plasticity prediction for a crystal with a slip system strength $\tau_0 = 50$ MPa. The distributions are shown on the deformed film (no magnification of the deformation).

crystal plasticity calculations. In particular, plasticity occurs only under the indenter in the continuum calculations. In the discrete dislocation calculations, slip emanates on the $\phi = \pm 35.3^\circ$ slip planes from the edge of the contact, and thus the plastic zone spreads outside the contact region.

The discrete dislocation calculations of the 50 μm film predict that the indentation pressure p decreases with increasing contact length (Fig. 6) for contact lengths less than about 4 μm. This indentation size effect has typically been attributed to geometrically necessary dislocations. The dislocation distributions at indentation depths $\delta = 0.2$ and 0.4 μm for the $\omega = 5^\circ$ wedge indentation of the $h = 50$ μm film are plotted in Fig. 8a and b, respectively. These dislocation distributions differ from what is assumed in an idealized model such as that of Nix and Gao (1998). One contribution to this difference is that the discrete dislocation calculations give rise to both statistically stored and geometrically necessary dislocations, but there is also a difference in the number and orientation of the slip systems.

The results for the $h = 2$ μm film are qualitatively different over the range of indentation depths considered here. For both the $\omega = 5^\circ$ and 10° indenters, the indentation pressure decreases with increasing contact length for $A < 2$ μm (corresponding to $\delta \approx 0.1$ and 0.2 μm for the $\omega = 5^\circ$ and 10° indenters, respectively). Subsequently, when the plastic zone reaches the substrate $x_2 = 0$, the indentation pressure increases with increasing contact length and no contact size-independent limit is reached. The discrete dislocation results indicate that the indentation pressure increases with increasing indentation depth for $\delta/h > 0.05$ and 0.1 for the $\omega = 5^\circ$ and 10° wedges, respectively. While the calculated indentation depths at which an increase in indentation pressure occurs are comparable to those seen experimentally by Han et al. (2006) and Saha et al. (2001), a quantitative comparison is not appropriate because the situation modeled here differs from that in the experiments in a variety of ways including differences in the indenter geometry and in the

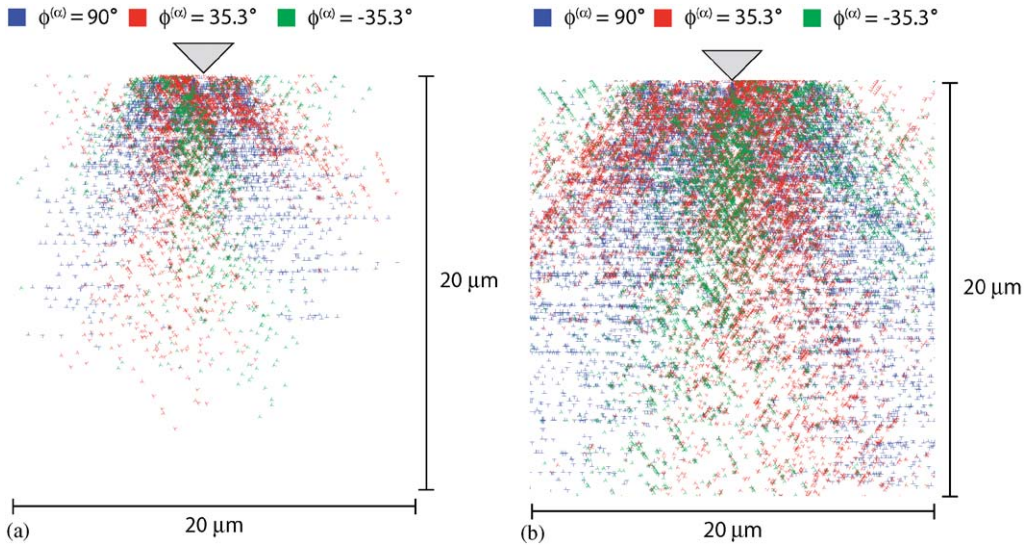

Fig. 8. The dislocation structure in a central 20 μm × 20 μm region around the indenter tip in the $h = 50$ μm film of the reference material indented to (a) $\delta = 0.2$ μm and (b) $\delta = 0.4$ μm by the $\omega = 5^\circ$ wedge.

elastic mismatch between the film and the substrate. Saha et al. (2001) have shown that appropriately calibrated strain gradient plasticity theories are capable of predicting this initial decrease and then increase in hardness with increasing indentation depth for the thin films, while conventional plasticity calculations significantly over-predict the indentation depths at which the plastic zone interacts with the substrate.

The variation of the nominal indentation pressure $p_N \equiv F/A_N$ with nominal contact length A_N is plotted in Fig. 9a and b for the $\omega = 5^\circ$ and 10° wedges, respectively. A comparison with Fig. 6 reveals that the nominal indentation pressure $p_N < p$ in the early stages of the indentation, especially for the $\omega = 10^\circ$ wedges. The trend reverses at large indentation depths for the $h = 2\,\mu m$ film when pile-up results in the actual contact length exceeding the nominal contact length. The discrete dislocation plasticity predictions of the p_N versus A_N relation for indentation of the $h = 50\,\mu m$ films at $\dot{\delta} = 0.04\,ms^{-1}$ are also included in Fig. 9. The nominal indentation pressure at the lower indentation rate is about 25% less than that at the reference indentation rate at small contact lengths. However, this difference is reduced to only about 5% lower at large contact lengths where the indentation pressure is essentially size independent.

The distribution of the stress σ_{22} under the $\omega = 5^\circ$ indenter in the $h = 2$ and $50\,\mu m$ films is plotted in Fig. 10a and b, respectively. These plots correspond to an indentation depth $\delta = 0.4\,\mu m$ and actual contact lengths $A \approx 12$ and $8\,\mu m$ for the $h = 2$ and $50\,\mu m$ films, respectively. In Fig. 10a, high compressive stresses are seen to develop beneath the contact zone while a tensile stress σ_{22} is generated at the edges of the contact zone. The stress distribution in the $h = 2\,\mu m$ film is clearly affected by the rigid substrate and is qualitatively different from the distribution in the $h = 50\,\mu m$ film.

We define the lattice rotation Ω as

$$\Omega = \tfrac{1}{2}(\hat{u}_{2,1} + \tilde{u}_{2,1} - \hat{u}_{1,2} - \tilde{u}_{1,2}), \tag{8}$$

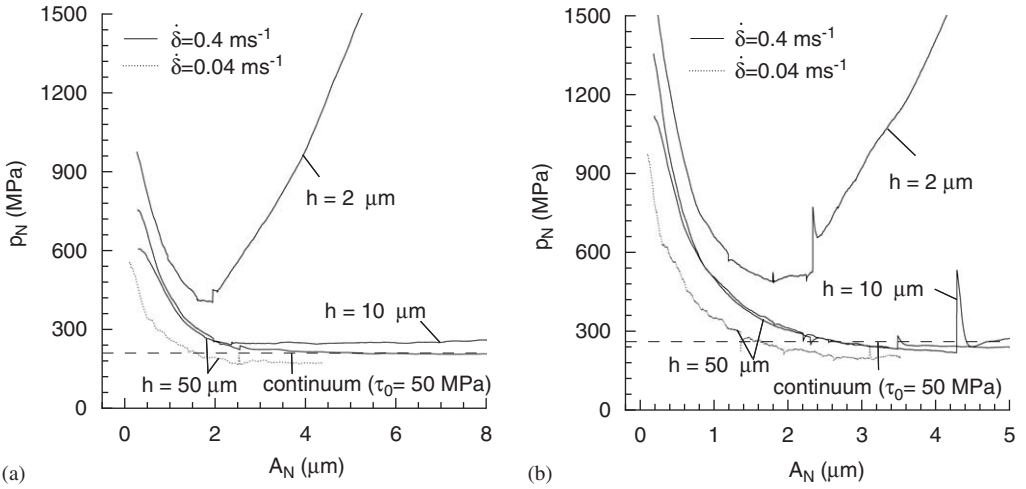

Fig. 9. The nominal indentation pressures p_N versus nominal contact length A_N for indentation of the reference material with the (a) $\omega = 5^\circ$ and (b) $\omega = 10^\circ$ wedges. Results are shown for three film thicknesses h. The continuum predictions of the nominal indentation pressures for a large crystal are also included.

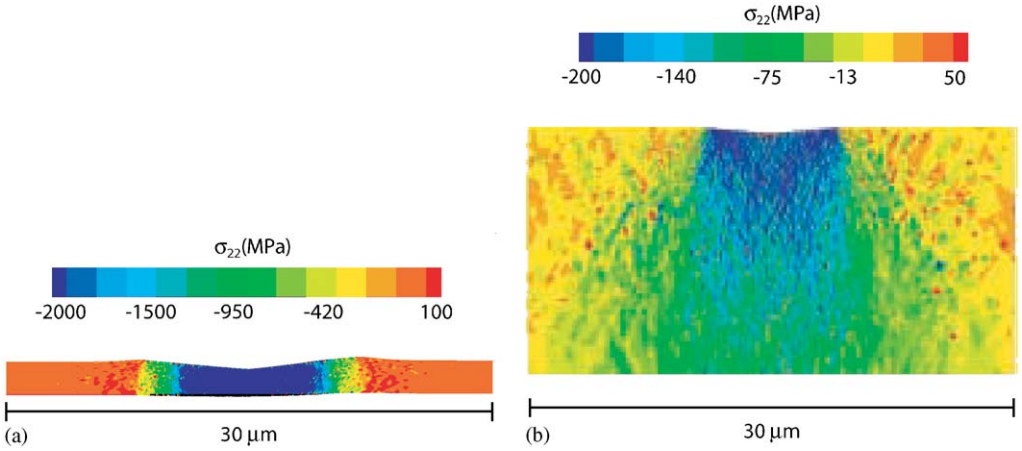

Fig. 10. The distribution of the stress σ_{22} in the (a) $h = 2\,\mu m$ and (b) $h = 50\,\mu m$ films of the reference material indented to $\delta = 0.4\,\mu m$ by the $\omega = 5^\circ$ wedge. The distributions are shown on the deformed film (no magnification of the deformation).

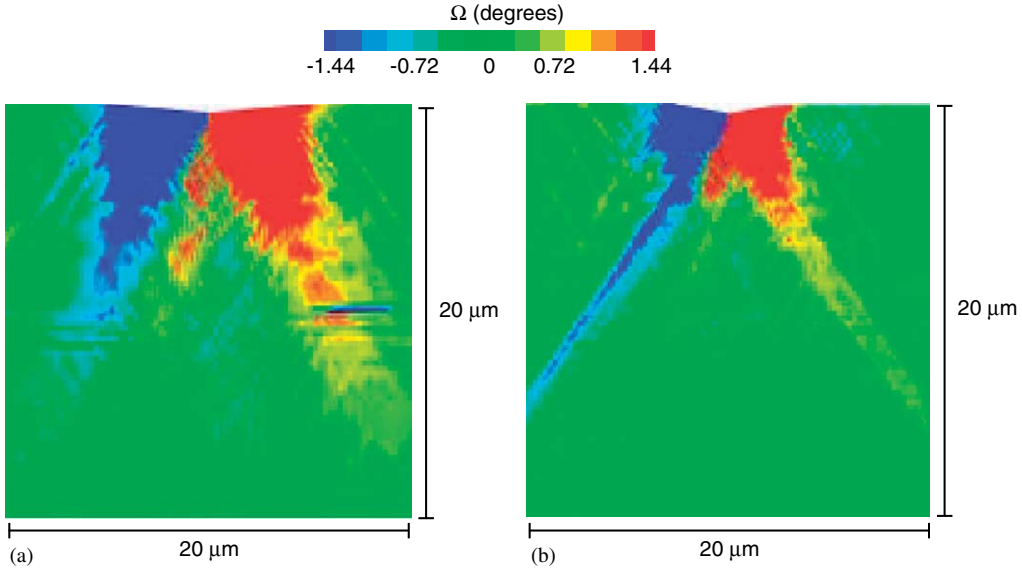

Fig. 11. The distribution of the lattice rotations under the indenter in the $h = 50\,\mu m$ film of the reference material indented to $\delta = 0.4\,\mu m$ by the (a) $\omega = 5^\circ$ and (b) $\omega = 10^\circ$ wedges. The distribution is shown in a central $20\,\mu m \times 20\,\mu m$ region around the indenter tip in the deformed film (no magnification of the deformation).

where the spatial differentiation $\tilde{u}_{i,j}$ is performed analytically to exclude the slip contribution of the ($\tilde{}$) fields. Contours of the lattice rotation Ω at $\delta = 0.4\,\mu m$ are plotted in Fig. 11a and b for indentation of the $h = 50\,\mu m$ film by the $\omega = 5^\circ$ and 10° indenters, respectively. As in the recent experimental results of Kysar et al. (2005) for $\omega = 45^\circ$ wedge indentation of copper single crystals, there is a rather abrupt change in the sign of the lattice rotation on the line $x_1 = 0$ immediately below the indenter. The continuum crystal

plasticity simulations of Bouvier and Needleman (2006), which assume symmetry about $x_1 = 0$, also predict a reasonably abrupt change in the sign of the lattice orientation.

4. Effect of source and obstacle density

In the indentation size effect observed in the results presented in Section 3 both strain gradients (and the consequent generation of geometrically necessary dislocations) imposed by the indentation process and source-limited plasticity (i.e. no available dislocation sources at locations of high stress) likely come into play. To explore the relative role of limited dislocation sources, we analyze indentation of a crystal with a lower density of dislocation sources.

The predicted indentation pressure p versus actual contact length A relation for the $\omega = 5^\circ$ indentation of the $h = 10$ and $50\,\mu\text{m}$ films of the LSD material ($\rho_{\text{src}} = 9\,\mu\text{m}^{-2}$, $\rho_{\text{obs}} = 18\,\mu\text{m}^{-2}$) is plotted in Fig. 12a. For comparison purposes, the corresponding results for the reference material (Fig. 6a) are also included. The indentation pressure is higher for the LSD crystal over the range of contact lengths considered here. While a contact size-independent indentation pressure was achieved for $A > 4\,\mu\text{m}$ in the reference material, a contact size-independent limit was not attained in the LSD material until $A > 8\,\mu\text{m}$. However, it does appear that the LSD and reference material responses converge to the same limit at large contact lengths. A comparison between the contact length A versus indentation depth δ relation for the $h = 10$ and $50\,\mu\text{m}$ films with the reference and LSD crystal properties is shown in Fig. 12b. The reduced plasticity in the LSD material results in increased material sink-in, though as for the indentation pressure results, the LSD and reference material curves appear to converge for large indentation depths. Although qualitatively the size-dependence of the reference and LSD crystals is similar, for a given indentation depth the indentation pressure of the LSD crystal is significantly greater than

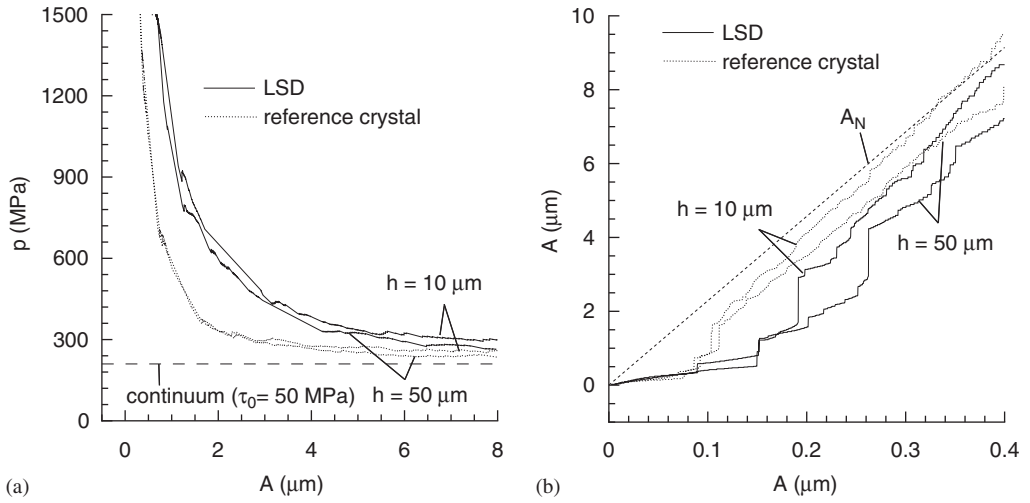

Fig. 12. A comparison between the $\omega = 5^\circ$ indentation of the reference ($\rho_{\text{src}} = 48\,\mu\text{m}^{-2}$, $\rho_{\text{obs}} = 98\,\mu\text{m}^{-2}$) and LSD ($\rho_{\text{src}} = 9\,\mu\text{m}^{-2}$, $\rho_{\text{obs}} = 18\,\mu\text{m}^{-2}$) films. (a) Actual indentation pressure versus actual contact length and (b) actual contact length as a function of indentation depth. Results are shown for the $h = 10$ and $50\,\mu\text{m}$ films.

that of the reference crystal. Thus, limited dislocation sources can provide a significant contribution to the indentation pressure at small indentation depths.

5. Comparison with the Nix–Gao model

Nix and Gao (1998) developed a model to capture the variation of the indentation pressure with indentation depth based on the role of geometrically necessary dislocations. They first calculated the density of geometrically necessary dislocations from geometric arguments and then employed the Taylor relation for the scaling of strength with dislocation density to derive the indentation pressure versus indentation depth relation as

$$\frac{p}{p_0} = \sqrt{1 + \frac{\delta^*}{\delta}}. \tag{9}$$

Here, δ^* is a characteristic length that depends on the wedge angle and p_0 is the indentation pressure in the infinite indentation depth limit. We note that in the Nix–Gao model neither p_0 nor δ^* are intrinsic material properties with $p_0 \propto \sqrt{\rho_s}$, where ρ_s is the density of statistically stored dislocations while the characteristic length δ^* depends on the statistically stored dislocation density through p_0 via the scaling relation $\delta^* \propto p_0^{-2}$.

The discrete dislocation plasticity predictions of the indentation pressure p versus indentation depth δ relation for the reference crystal indented by the $\omega = 5^\circ$ wedge is plotted in Fig. 13 for the three film thicknesses considered. We observe that the indentation pressure drops sharply at $\delta \approx 0.1\,\mu m$. For the two thicker films, the indentation pressure then decreases smoothly with increasing δ before leveling off at $\delta \approx 0.4\,\mu m$. The very high indentation pressures at $\delta < 0.1\,\mu m$ are a result of the fact that the actual contact length remains nearly unchanged in the range $0 \leqslant \delta \leqslant 0.1\,\mu m$ (Fig. 4a). It is clear from Fig. 13 that Eq. (9) will not provide a good fit to the discrete dislocation predictions of the actual indentation pressure versus δ relation.

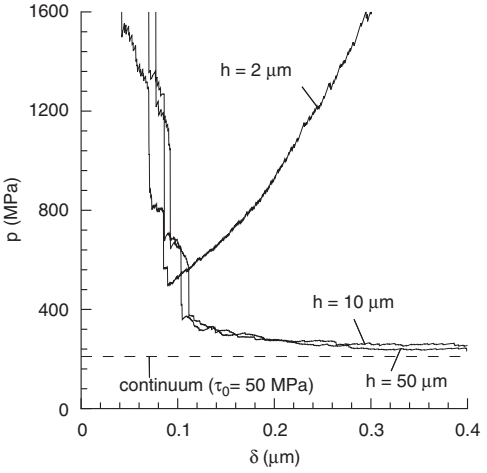

Fig. 13. Discrete dislocation predictions of the indentation pressure p versus indentation depth δ relation of the reference material. Results are shown for three selected film thicknesses h.

However, we proceed to demonstrate that the discrete dislocation predictions of the nominal indentation pressure versus indentation depth are reasonably well represented by the Nix and Gao (1998) relation. The nominal indentation pressure versus indentation depth predictions for the $\omega = 5^\circ$ and 10° wedge indentation of the $h = 50\,\mu\text{m}$ films of the reference material are plotted in Fig. 14a. The best fits to the discrete dislocation predictions using the relation Eq. (9) (with p_0 and δ^* as free parameters given by a least-squares fit) are included in Fig. 14a, with the values of the parameters listed in Table 1. Note that Eq. (9) is fit to the "plastic" part of the p_N versus δ curve and then back-extrapolated to the smaller indentation depths as shown in Fig. 14a. The Nix and Gao (1998) relation fits the discrete dislocation predictions reasonably well. However, the best-fit parameters for the $\omega = 10^\circ$ indenter have a value of p_0 much lower than the value given by a continuum plasticity calculation. Moreover, the value obtained for the material length scale δ^* is 4.9 μm: this is much larger than the slip plane spacing or the dislocation source and obstacle spacings and is not clearly related to any physical material length scale of the reference material.

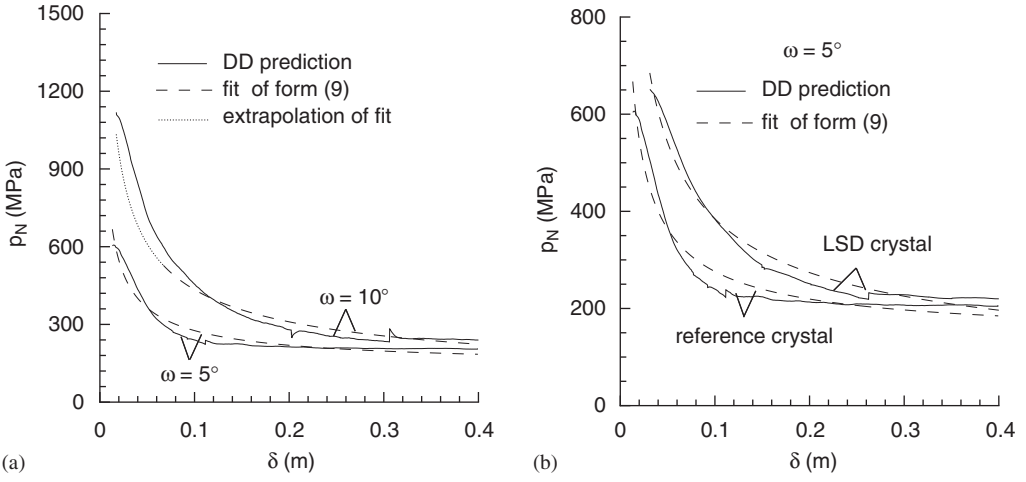

Fig. 14. Comparisons between the discrete dislocation predictions for the indentation of the $h = 50\,\mu\text{m}$ films and best fits of the Nix–Gao relation Eq. (9) (the parameter values are given in Table 1) for (a) the $\omega = 5^\circ$ and 10° indentation of the reference crystals and (b) the $\omega = 5^\circ$ indentation of the LSD and reference crystals.

Table 1
The parameters used to plot Eq. (9) in Fig. 14

Material	Wedge angle ω (deg.)	Parameters for Eq. (9)		Parameters for Eq. (10)		
		p_0 (MPa)	δ^* (μm)	p_0 (MPa)	δ^* (μm)	n
Reference	5	142	0.28	163	0.10	0.70
Reference	10	61	4.9	107	0.84	0.64
LSD	5	47	6.7	131	0.37	0.68

The best-fit parameters for Eq. (10) are also included.

In order to determine whether a power-law exponent other than 0.5 gives a more appropriate fit to the discrete dislocation results, we consider a relation of the form

$$\frac{p_N}{p_0} = \left(1 + \frac{\delta^*}{\delta}\right)^n. \tag{10}$$

Using the parameters listed in Table 1, this relation gives fits nearly identical to those shown in Fig. 14a. Interestingly, with power-law exponents $n \approx 0.65$–0.7 the best-fit value for p_0 is closer to the continuum crystal plasticity prediction than when n is fixed at 0.5 and δ^* is of the order of the source and obstacle spacings in the material.

The nominal indentation pressure versus indentation depth predictions for the $\omega = 5^\circ$ wedge indentation of the $h = 50\,\mu m$ films with the reference as well as with the LSD crystal properties are plotted in Fig. 14b along with the best fits of Eq. (9) (the fitting parameters are listed in Table 1). The best-fit parameters for the LSD material using Eq. (10) are also listed in Table 1. For the LSD crystals with $n > 0.5$, the parameter p_0 also has a value that is representative of its large indentation depth value and δ^* has a greater value than for the reference material, indicating that δ^* increases with the average dislocation source and obstacle spacings.

The linear dependence of the square of the indentation pressure $(p/p_0)^2$ with the inverse indentation depth $1/\delta$ as predicted by Nix and Gao (1998) is in good agreement with a wide body of experimental evidence for indentation depths $\delta > 1\,\mu m$. But the fit over a wider range of indentation depths is not as good; see, for example, Poole et al. (1996), Gerberich et al. (2002) and Swadener et al. (2002). This is consistent with the conical indentation simulations of Begley and Hutchinson (1998) using the Fleck and Hutchinson (1997) strain gradient plasticity theory which do not predict the Nix and Gao (1998)-type scaling over the full range of indentation depths. Begley and Hutchinson (1998) suggested that alternative descriptions of the effective strain (which governs the interaction between the statistical and geometrically necessary dislocations) in the Fleck and Hutchinson (1997) strain gradient plasticity model could be employed to obtain the Nix and Gao (1998)-type scaling. Recently, Abu Al-Rub and Voyiadjis (2004) have proposed a form of the effective strain relation in the Fleck and Hutchinson (1997) model that does indeed reproduce the Nix and Gao (1998) scaling relation. Huang et al. (2006) have proposed an extension of the Nix–Gao model based on the assumption that there exists a maximum allowable density of geometrically necessary dislocations.

The discrete dislocation results suggest that exponents in the range 0.6–0.7, rather than 0.5 as in Eq. (9), are more suitable for describing the indentation size effect in the present calculations. There are several possible reasons for this including: (i) the current two-dimensional discrete dislocation plasticity simulations do not give rise to the square root Taylor relation on which Eq. (9) is based, although this can be included by using the extended set of constitutive rules suggested by Benzerga et al. (2004); (ii) the indentation depths in the calculations presented here are restricted to $\delta \leqslant 0.4\,\mu m$ and, as discussed by Abu Al-Rub and Voyiadjis (2004), the Nix and Gao (1998) model is most appropriate for indentation depths $\delta > 1\,\mu m$; (iii) the models of Nix and Gao (1998) and of Huang et al. (2006) essentially assume no interaction between the statistically stored and geometrically necessary dislocations and this interaction occurs naturally in the discrete dislocation plasticity calculations; (iv) the Nix and Gao (1998) and Huang et al. (2006) models assume a hemispherical plastic zone with a radius equal to the nominal contact radius and the single crystal discrete dislocation calculations (see Fig. 7a) give a much larger plastic zone size; and

(v) the calculations here are carried out for wedge angles ω smaller than representative of typical indenters used in the experiments and the discrete dislocation calculations suggest that the best-fit exponent n decreases somewhat with increasing wedge angle.

6. Estimation of the contact area

Experimentally, measuring the true contact area is difficult, if not impossible. To avoid the need for the determination of true contact area, the hardness is sometimes identified with the nominal indentation pressure p_N, rather than true indentation pressure (Ma and Clarke, 1995; Poole et al., 1996). The results here (see Figs. 6 and 9) indicate that sink-in occurs in the size regime where there is a significant size-dependent increase in hardness. Hence, the indentation size effect of the increasing indentation pressure with decreasing contact size might be even more significant than that suggested by the experiments as sink-in during the early stages of the indentation results in the actual contact length being less than the nominal contact length. In other circumstances, an unloading procedure suggested by Oliver and Pharr (1992) (also see Oliver and Pharr (2004) for a review of various refinements to the original method) is used which is based on the assumption that the sink-in can be modeled by elastic indentation of a half-space by a rigid punch having a simple geometry. In particular, the sink-in δ_s (see Fig. 1b) at an indentation load F_{max} is given by (Oliver and Pharr, 1992)

$$\delta_s = \eta \frac{F_{max}}{S}, \tag{11}$$

where $S \equiv dF/d\delta|_{F=F_{max}}$ is the initial slope of the unloading curve from F_{max} and η is a non-dimensional constant that depends on the geometry of the indenter and the film thickness. The procedure then is to determine the initial unloading stiffness S from experimental measurements, extract δ_s from Eq. (11) and estimate the actual contact length A at the indentation load F_{max} via the geometrical relation

$$A = \frac{2(\delta_{max} - \delta_s)}{\tan \omega}. \tag{12}$$

The procedure of Oliver and Pharr (1992) has been shown to hold for the indentation of solids modeled by conventional isotropic continuum plasticity, see, for example, Cheng and Cheng (1997). Here, we explore the extent to which this procedure can estimate the actual contact length A in the discrete dislocation plasticity indentation calculations.

Fig. 15a shows the unloading response from six indentation depths in the $h = 50\,\mu m$ film with the reference crystal properties for the $\omega = 5^\circ$ indenter. The predictions for the initial unloading response from six selected values of the indentation force are also included in Fig. 15a. These unloading simulations were carried out at an unloading rate $\dot{\delta} = -0.4\,ms^{-1}$ with nodes stuck to the rigid indenter released from the contact when the inter-facial traction T_2 becomes tensile. The initial unloading stiffness S is estimated from these calculations and the discrete dislocation plasticity predictions of the variation of the sink-in δ_s (calculated from Eq. (12) as the actual contact area A is known directly from the simulation) at $F = F_{max}$ with F_{max}/S is plotted in Fig. 15b. Here, F_{max} is the indentation load at the onset of unloading. In addition, the prediction of the δ_s versus F_{max}/S relation from an elastic calculation of the $\omega = 5^\circ$ wedge indentation of the $h = 50\,\mu m$ film is also included in Fig. 15b and these finite element calculations suggest that the proportionality

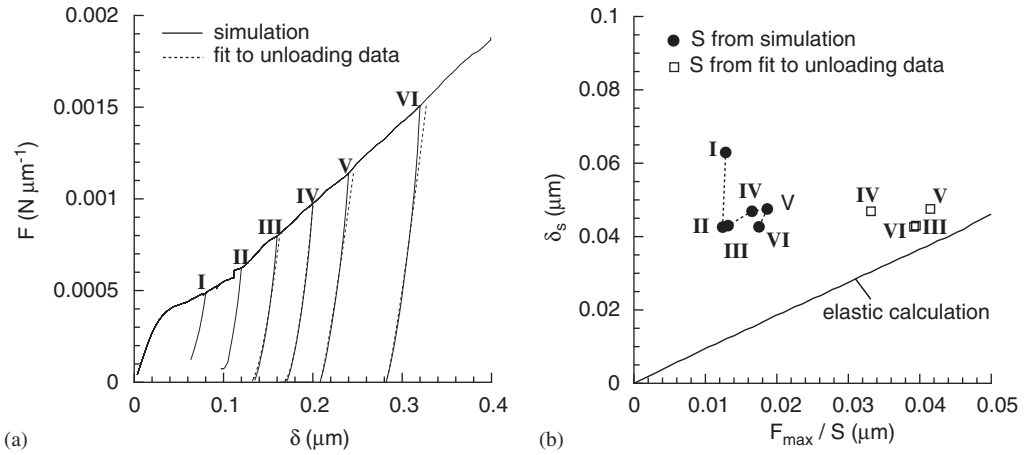

Fig. 15. (a) The loading and unloading indentation force versus depth predictions for the $h = 50\,\mu\text{m}$ film by the $\omega = 5^\circ$ indenter and (b) the variation of the sink-in depth δ_s with the initial unloading stiffness S.

Table 2
The parameters used to fit Eq. (13) to the unloading discrete dislocation predictions in Fig. 15a

Unloading curve	α $\text{N}\,\mu\text{m}^{-(m+1)}$	m	Correlation coefficient, R
III	0.0350	1.21	0.8814
IV	0.1004	1.48	0.8961
V	0.0486	1.14	0.9947
VI	0.0597	1.19	0.9961

constant in Eq. (11) $\eta \approx 0.92$. The discrete dislocation plasticity calculations do not predict a linear scaling of δ_s with $F_{\max}/S$ as required by Eq. (11) and predicted by the elastic finite element calculations. In fact, over the range of indentation depths considered in Fig. 15b, the calculations suggest that δ_s is relatively independent of $F_{\max}/S$.

As in experiments, the determination of S from F–δ curves in the simulations tends to be inaccurate. As a work-around, Oliver and Pharr (1992) suggest fitting a relation of the form

$$F = \alpha(\delta - \delta_f)^m, \tag{13}$$

to the unloading curves and then estimating the initial unloading stiffness as

$$S \equiv \left(\frac{dF}{d\delta}\right)_{\delta=\delta_{\max}} = \alpha m(\delta_{\max} - \delta_f)^{m-1}. \tag{14}$$

Here, δ_f is the residual indentation depth upon complete unloading while $\delta_{\max}$ is the indentation depth at which unloading commenced. We fit Eq. (13) to some of the discrete dislocation plasticity predictions of the unloading curves using a least-squares fit. These fits are included in Fig. 15a as dashed lines and the corresponding fitting parameters are listed in Table 2 (along with the correlation coefficient R). As in the experimental observations

reported by Oliver and Pharr (1992), the predicted power-law exponents are in the range $m = 1.1$–1.4. The F_{max}/S versus δ_s relation predicted by fitting Eq. (13) to the discrete dislocation calculations is included in Fig. 15b with open symbols. The fitting procedure of Oliver and Pharr (1992) also does not give results consistent with the elastic scaling relation Eq. (11), although the agreement is better than obtained using the direct estimate of S obtained from the unloading discrete dislocation calculations.

The discrepancy between Eq. (11) and the discrete dislocation predictions could arise from: (i) material sink-in in these calculations is not solely due to elastic deformations, i.e. the dislocations affect material sink-in and (ii) unloading is not purely elastic in the discrete dislocation calculations.

In order to illustrate the occurrence of reverse plasticity, the evolution of the dislocation density with indentation depth for the $\omega = 5^\circ$ indentation of the $h = 50\,\mu m$ film is plotted in Fig. 16a. Here, the dislocation density is the number of dislocations per unit area in a region extending 25 μm on each side of the indenter tip and the 50 μm through the film thickness. The data for the evolution of the dislocation density during unloading are also included in Fig. 16a for the six unloading simulations performed. The figure clearly shows that significant dislocation activity occurs during the initial unloading period with the dislocation density increasing during unloading. This "reverse plasticity" is more significant for unloading from the larger indentation loads and contributes to the disagreement of the discrete dislocation predictions with Eq. (11). It is worth noting that the two-dimensional discrete dislocations calculations may overestimate the effect of reverse plasticity. Three-dimensional discrete dislocations simulations are needed in order to ascertain whether or not the effect obtained here is an overestimate.

While the discrete dislocation predictions are not in agreement with Eq. (11), the main aim of the Oliver and Pharr (1992) procedure is to estimate the actual contact length A.

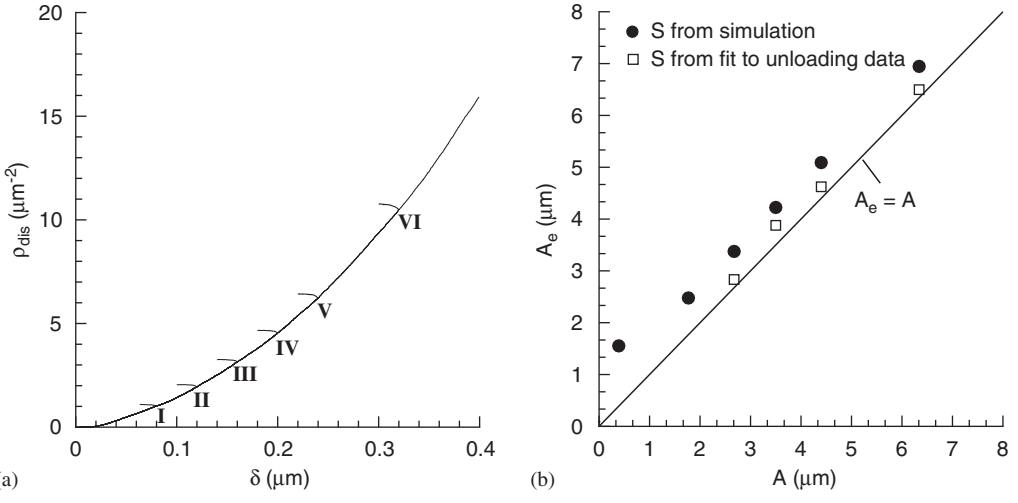

Fig. 16. Discrete dislocation plasticity predictions for the indentation of the $h = 50\,\mu m$ film of the reference material by the $\omega = 5^\circ$ indenter. (a) Predictions of the evolution of the dislocation density with indentation depth. The evolution of the dislocation density for unloading from the six selected points marked in Fig. 15a are also included. (b) A comparison between the estimated contact length A_e with the actual contact length A.

Here an estimated contact length, A_e, is calculated in two ways: (i) the unloading stiffness S is estimated directly from the discrete dislocation calculations; and (ii) the value of S is obtained from the fit Eq. (13). In both cases, the line labeled "elastic calculation" in Fig. 15b is used to obtain δ_s for a given F_{max}/S. This value of δ_s is then used in Eq. (12) to calculate the estimated contact length A_e. A comparison between the estimated contact length, A_e, and the actual contact length, A, is shown in Fig. 16b for the $\omega = 5^\circ$ indentation of the $h = 50\,\mu m$ film with the reference crystal properties (no estimate based on the fitting relation Eq. (13) is shown for the first two points because the unloading calculations for these were not continued to zero indentation pressure). In both cases, the estimated contact length exceeds the actual contact length though the discrepancy is small when the fit Eq. (13) is employed to determine S. At least in the cases considered here, the Oliver and Pharr (1992) procedure using the power-law fit Eq. (13) together with an elastic analysis provides a good estimate of the actual contact area even though the initial unloading stiffness is not accurately represented.

7. Conclusions

We have carried out plane strain analyses of the indentation of single crystal films by rigid wedge-shaped indenters. While the computations are carried out within a small-strain framework, contact is modeled by considering the deformed surface profile of the films. Films with thicknesses h of 2, 10 and 50 μm were analyzed. The crystals are initially dislocation-free with dislocation nucleation occurring from Frank–Read sources of a specified density, randomly distributed in the crystal. The discrete dislocation calculations predict:

- When the film thickness is sufficiently large relative to the indentation depth, the indentation pressure decreases with increasing contact length. For sufficiently thick films, with both the reference and low dislocation source density (LSD) crystal properties, a size-independent indentation pressure is attained as the indentation depth increases. This contact size-independent indentation pressure is in good agreement with the prediction of conventional continuum crystal plasticity theory. For small contact depths, the indentation pressure with the LSD crystal properties is significantly greater than with the reference crystal properties.
- For films with $h = 2\,\mu m$, the indentation pressure initially decreases with increasing contact length and then increases with contact size when the plastic zone reaches the rigid substrate. This occurs at an indentation depth of $\delta/h \approx 0.04$ and 0.1 for the $\omega = 5^\circ$ and 10° wedges, respectively.
- Over the range of indentation depths considered, material sink-in is predicted for the 10 and 50 μm films, while material pile-up occurs for the $h = 2\,\mu m$ film when the plastic zone reaches the substrate. With sink-in the actual indentation pressure is typically greater than the nominal indentation pressure, but this is reversed for the $h = 2\,\mu m$ film when pile-up occurs.
- The nominal indentation pressure versus depth relation can be described by power-law relation in one of two ways: (i) with a power-law exponent of 0.5 as in Nix and Gao (1998); or (ii) with a best-fit power-law exponent ranging between 0.6 and 0.7. With the best-fit power-law exponent, the parameters in the relation have values on the order of physically identifiable quantities—the continuum crystal plasticity limit for the

indentation pressure and the dislocation source and obstacle spacings for the characteristic length. The value of the characteristic length also increases with increasing wedge angle.

- Over the range of parameters considered in the plane strain analyses here, neither the initial unloading slope nor the amount of material sink-in are accurately modeled using estimates based on a conventional continuum analysis. However, the actual (but not accounting for any effect of surface roughness) contact area is well-modeled by an elastic unloading analysis in conjunction with the fitting procedure of Oliver and Pharr (1992).

Finally, we note that at a sufficiently small scale, dislocation nucleation from surfaces, in particular from surface steps, as presumed in the model of Hurtado and Kim (1999a, b) may play a prominent role. At present, no criterion has been developed for surface-step dislocation nucleation that is appropriate for use in a discrete dislocation plasticity formulation. The development of such a criterion and an analysis accounting for the possibility of both surface and bulk dislocation nucleation would be a significant additional step.

Acknowledgments

D.S.B. and V.S.D. acknowledge support from the Leverhulme Trust, UK. A.N. is pleased to acknowledge support from the Materials Research Science and Engineering Center at Brown University (NSF Grant DMR-0520651).

References

Abu Al-Rub, R.K., Voyiadjis, G.Z., 2004. Analytical and experimental determination of the material intrinsic length scale of strain gradient plasticity theory from micro- and nano-indentation experiments. Int. J. Plasticity 20, 1139–1182.

Begley, M.R., Hutchinson, J.W., 1998. The mechanics of size-dependent indentation. J. Mech. Phys. Solids 46, 2049–2068.

Benzerga, A.A., Bréchet, Y., Needleman, A., der Giessen, E.V., 2004. Incorporating three-dimensional mechanisms into two-dimensional dislocation dynamics. Modelling Simulation Mater. Sci. Eng. 12, 159–196.

Bhattacharya, A.K., Nix, W.D., 1988. Analysis of elastic and plastic deformation associated with indentation testing of thin films on substrates. Int. J. Solids Struct. 24, 1287–1298.

Bouvier, S., Needleman, A., 2006. Effect of the number and orientation of active slip systems on plane strain single crystal indentation. Modelling Simulation Mater. Sci. Eng., submitted for publication.

Cheng, C.M., Cheng, Y.T., 1997. On the initial unloading slope in indentation of elastic–plastic solids by an indenter with an axisymmetric smooth profile. Appl. Phys. Lett. 71, 2623–2625.

Cleveringa, H.H.M., Van der Giessen, E., Needleman, A., 1999. A discrete dislocation analysis of bending. Int. J. Plasticity 15, 837–868.

Deshpande, V.S., Needleman, A., Van der Giessen, E., 2005. Plasticity size effects in tension and compression of single crystals. J. Mech. Phys. Solids 53, 2661–2691.

Fivel, M.C., Robertson, C.F., Canova, G.R., Boulanger, L., 1998. Three-dimensional modeling of indent-induced plastic zone at a mesoscale. Acta Mater. 46, 6183–6194.

Fleck, N.A., Hutchinson, J.W., 1997. Strain gradient plasticity. In: Hutchinson, J.W., Wu, T.Y. (Eds.), Advances in Applied Mechanics, vol. 33. Academic Press, New York, p. 296.

Freund, L.B., 1994. The mechanics of dislocations in strained-layer semiconductor-materials. Adv. Appl. Mech. 30, 1–66.

Freund, L.B., Suresh, S., 2004. Thin Film Materials: Stress, Defect Formation and Surface Evolution. Cambridge University Press, Cambridge, UK.

Gerberich, W.W., Tymiak, N.I., Grunlan, J.C., Horstemeyer, M.F., Baskes, M.I., 2002. Interpretations of indentation size effects. J. Appl. Mech. 69, 433–442.

Gouldstone, A., Koh, H.J., Zeng, K.Y., Giannakopoulos, A.E., Suresh, S., 2000. Discrete and continuous deformation during indentation of thin films. Acta Mater. 48, 2277–2295.

Han, S.M., Saha, R., Nix, W.D., 2006. Determining hardness of thin films in elastically mismatched film-on-substrate systems using nanoindentation. Acta Mater. 54, 1571–1581.

Horstemeyer, M.F., Baskes, M.I., Plimpton, S.J., 2001. Computational nanoscale plasticity simulations using embedded atom potentials. Theor. Appl. Fract. Mech. 37, 49–98.

Huang, Y., Zhang, F., Hwang, K.C., Nix, W.D., Pharr, G.M., Feng, G., 2006. A model of size effects in nano-indentation. J. Mech. Phys. Solids 54, 1668–1686.

Hurtado, J.A., Kim, K.-S., 1999a. Scale effects in friction of single-asperity contacts I. From concurrent slip to single-dislocation-assisted slip. Proc. R. Soc. London A 455, 3363–3384.

Hurtado, J.A., Kim, K.-S., 1999b. Scale effects in friction of single-asperity contacts II. Multiple-dislocation-cooperated slip. Proc. R. Soc. London A 455, 3385–3400.

Johnson, K.L., 1970. The correlation of indentation experiments. J. Mech. Phys. Solids 18, 115–126.

Kreuzer, H.G.M., Pippan, R., 2004. Discrete dislocation simulation of nanoindentation. Comput. Mech. 33, 292–298.

Kreuzer, H.G.M., Pippan, R., 2005. Discrete dislocation simulation of nanoindentation: the effect of statistically distributed dislocations. Mater. Sci. Eng. A 400–401, 460–462.

Kysar, J.W., Gan, Y.X., Morse, T.L., Chen, X., Huh, W.T., 2005. Indentation of face-centered cubic crystals: measurement of lattice rotation and geometrically necessary dislocation density, in preparation.

Lou, J., Shrotriya, P., Buchheit, T., Yang, D., Soboyejo, W.O., 2003. Nanoindentation study of plasticity length scale effects in LIGA Ni microelectromechanical systems structures. J. Mater. Res. 18, 719–728.

Ma, Q., Clarke, D.R., 1995. Size dependent hardness of silver single crystals. J. Mater. Res. 10, 853–863.

Miller, R.E., Shilkrot, L.E., Curtin, W.A., 2004. A coupled atomistics and discrete dislocation plasticity simulation of nanoindentation into single crystal thin films. Acta Mater. 52, 271–284.

Nix, W.D., Gao, H., 1998. Indentation size effects in crystalline materials: a law for strain gradient plasticity. J. Mech. Phys. Solids 43, 411–423.

Oliver, W.C., Pharr, G.M., 1992. An improved technique for determining hardness and elastic-modulus using load and displacement sensing indentation experiments. J. Mater. Res. 7, 1564–1583.

Oliver, W.C., Pharr, G.M., 2004. Measurement of hardness and elastic modulus by instrumented indentation: advances in understanding and refinements to methodology. J. Mater. Res. 19, 3–20.

Polonsky, I.A., Keer, L.M., 1996. Simulation of microscopic elastic–plastic contacts by using discrete dislocations. Proc. R. Soc. London A 452, 2173–2194.

Poole, W.J., Ashby, M.F., Fleck, N.A., 1996. Micro-hardness of annealed and work-hardened copper polycrystals. Scr. Mater. 34, 559–564.

Qu, S., Huang, Y., Pharr, G.M., Hwang, K.C., 2006. The indentation size effect in the spherical indentation of iridium: a study via the conventional theory of mechanism-based strain gradient plasticity. Int. J. Plasticity 22, 1265–1286.

Rice, J.R., 1987. Tensile crack tip fields in elastic ideally plastic crystals. Mech. Mater. 6, 317–335.

Saha, R., Xue, Z., Huang, Y., Nix, W.D., 2001. Indentation of a soft metal film on a hard substrate: strain gradient hardening effects. J. Mech. Phys. Solids 49, 1997–2014.

Swadener, J.G., George, E.P., Pharr, G.M., 2002. The correlation of the indentation size effect measured with indenters of various shapes. J. Mech. Phys. Solids 50, 681–694.

Tabor, D., 1951. Hardness of Metals. Clarendon Press, Oxford, UK.

Van der Giessen, E., Needleman, A., 1995. Discrete dislocation plasticity: a simple planar model. Modelling Simulation Mater. Sci. Eng. 3, 689–735.

Wei, Y., Hutchinson, J.W., 2003. Hardness trends in micron scale indentation. J. Mech. Phys. Solids 51, 2037–2056.

Widjaja, A., Van der Giessen, E., Needleman, A., 2005. Discrete dislocation modelling of submicron indentation. Mater. Sci. Eng. A 400–401, 456–459.

Widjaja, A., Needleman, A., Deshpande, V.S., VanderGiessen, E., 2006. On contact and size effects in discrete dislocation modelling of wedge indentation, submitted for publication.

Zhu, T., Li, J., Van Vliet, K.J., Yip, S., Suresh, S., 2003. Simulation of nanoindentation via interatomic potential finite element method. Comput. Fluid Solid Mech. 1–2, 795–799.